

Cite this: *RSC Adv.*, 2017, **7**, 45470

Ion exchange-prepared NaSbSe_2 nanocrystals: electronic structure and photovoltaic properties of a new solar absorber material

Belete Asefa Aragaw,^{ab} Jifeng Sun,^c David J. Singh^{cd} and Ming-Way Lee^{id}*^a

We report the calculated electronic structure, syntheses and photovoltaic properties of a new ternary solar absorber material NaSbSe_2 . NaSbSe_2 nanocrystals (NCs) have been prepared from a $\text{Na}-\text{Sb}-\text{S}$ precursor by the solution-based Se^{2-} anion exchange reaction. The $\text{Na}-\text{Sb}-\text{S}$ precursor was grown on a TiO_2 electrode using the successive ionic layer adsorption and reaction (SILAR) method. X-ray diffraction shows that the synthesized NaSbSe_2 NCs have the same crystal structure as the NaSbS_2 precursor with the diffraction angles significantly down-shifted. Energy-dispersive X-ray spectroscopy confirms the complete anion exchange and formation of the NaSbSe_2 phase. First principles calculations show that the ordered NaSbSe_2 structure resulting from the ion exchange synthesis is important for the performance. The NaSbSe_2 NCs have an average size of ~ 17 nm and a near-optimal optical band gap E_g of 1.48 eV that is lower than the NaSbS_2 precursor. Liquid-junction NaSbSe_2 quantum dot-sensitized solar cells (QDSSCs) were fabricated from the synthesized NaSbSe_2 NCs for the first time. The best cell, prepared using the Au counter electrode and the polysulfide electrolyte, yielded an efficiency of 2.22%, a short current density of 1.31 mA cm^{-2} , an open-circuit voltage of 0.30 V and a fill factor of 56.4% under the reduced light intensity of 10% sun. The external quantum efficiency (EQE) spectrum covers the spectral range of 300–900 nm with a maximum EQE of 75% at $\lambda = 500$ nm. The near-optimal E_g suggests that NaSbSe_2 could be a potential material for solar cells. In addition, the ion exchange method can be extended to the preparation of many new metal selenide-based solar materials from their corresponding sulfides. These materials may show improved characteristics compared to samples with more disorder.

Received 21st June 2017
 Accepted 15th September 2017

DOI: 10.1039/c7ra06938c
rsc.li/rsc-advances

1. Introduction

Dye-sensitized solar cells (DSSCs) are emerging as a candidate for the next generation of low-cost alternatives to Si photovoltaic devices. Their benefits include solution processing, ease of fabrication, and low costs. Due to the limitations of dye absorbers on the bandwidth of light harvesting as well as synthesis of new and low-cost dyes, inorganic semiconductor quantum dot solar absorbers have acquired increasing attention. Semiconductor quantum dot-sensitized solar cells (QDSSCs), derived on the same principle of a DSSC, are more promising due to the unique properties of semiconductor quantum dot solar absorbers such as band gap tunability and high extinction coefficient.^{1–5} Moreover, the multiple exciton generation effect in a quantum dot could push the Shockley–Queisser theoretical efficiency limit of 31% to 44% for single band gap solar cells.⁶

Ternary semiconductors based on metal chalcogenides have a broader range of electrical and optical properties than either the elementary or binary compounds because of the possibility of varying the constituent elements and their compositions. One of the representative ternary semiconductors – the I–V–VI₂ class, where I = Cu, Ag, or alkali metals; V = Sb, Bi; and VI = S, Se, Te, have been studied for their potential applications in thermoelectrics^{7–10} and solar cells.^{11–16} Among the various I metals, the Cu-based I–V–VI₂ materials, such as Cu–Bi–S, CuSbS₂, have been explored as solar materials.^{17–21} The Ag-based materials such as AgSbS₂, Ag₃SbS₃, and AgBiS₂ have also been reported recently.^{11,16,22} In contrast, I–V–VI₂ materials based on alkali metals have been rarely investigated despite their ease of preparation and promising solar cell performance.²³ Alkali metal antimony-based ternary chalcogenides of the type A^ISbX₂^{VI} (where A = Na, K, Rb and X = S, Se) had been synthesized by the direct interaction of an alkali metal with antimony and either sulphur or selenium at extremely high temperature.^{24–26} The cation sublattice of these compounds is often disordered at high temperature and may order or partially order as temperature is lowered.

Recently a member of the alkali antimony A^ISbX₂^{VI} group – NaSbS₂ – has been demonstrated as a potential solar material, achieving a power conversion efficiency of 3.2% under the

^aInstitute of Nanoscience and Department of Physics, National Chung Hsing University, Taichung 402, Taiwan. E-mail: mwl@phys.nchu.edu.tw

^bDepartment of Chemistry, Bahir Dar University, P.O. Box 79, Bahir Dar, Ethiopia

^cDepartment of Physics and Astronomy, University of Missouri, Columbia, MO 65211-7010, USA



reduced light intensity of 0.1 sun.²³ First-principles calculations indicate that the particular electronic structure, which has hybridization between Sb and S p-states of NaSbS_2 , could provide screening and defect tolerance for carrier collection, making NaSbS_2 a potential solar material.²⁷ Replacing the S element with the heavier Se element lowers the energy gap E_g from 1.8 (NaSbS₂) to 1.6 eV (NaSbSe₂), as reported by Bazakutsa *et al.*²⁴ based on measurements on thin film samples. The reduced E_g would lead to a broader optical absorption band, suggesting that NaSbSe₂ would have better light harvesting ability than that of NaSbS₂, which is a favorable property for a solar material. In addition, NaSbSe₂ has a large absorption coefficient of $\alpha = 10^5 \text{ cm}^{-1}$ at $\lambda = 600 \text{ nm}$.²⁴ The broad absorption band and large absorption coefficient suggests that NaSbSe₂ could be a potential solar absorber material. Moreover, the three elements contained in NaSbSe₂ are earth-abundant, low cost, nontoxic and environmentally friendly. However, there has been no report on solar cells based on NaSbSe₂ so far. Thin films of NaSbSe₂ had been synthesized by thermal evaporation.²⁴ Here NaSbSe₂ nanocrystals (NCs) were produced by selenide ion exchange from a successive ionic layer adsorption reaction (SILAR)-prepared Na-Sb-S precursor. First principles calculations comparing ordered and disordered cation sub-lattices show that this synthesis method is important as cation disorder reduces the optical band gap to below the useful range. Liquid-junction quantum dot-sensitized solar cells based on NaSbSe₂ are demonstrated for the first time. We investigate the effects of ion exchange time and the number of SILAR cycles on the optical spectra and photovoltaic performance of NaSbSe₂. We also investigate the dependence of photovoltaic parameters on the types of counter electrode. The best cell yielded an efficiency of 2.2%, a respectable efficiency for the first report of a new solar material.

2. Experimental

2.1 Materials and methods

Preparation of TiO_2 photoelectrode. Fluorine-doped tin oxide glass (FTO, Pilkington, sheet resistance $\sim 7 \Omega \square^{-1}$) was cut to $1.2 \times 2.0 \text{ cm}^2$ pieces, followed by cleaning with acetone, methanol and deionized water consecutively for 5 min each under ultrasonic bath. Three layers of TiO_2 films with different particle sizes and film thicknesses were coated layer-by-layer on the FTO substrate. First, a blocking or compact layer of TiO_2 ($\sim 90 \text{ nm}$ thick) was made by spin-coating (2000 rpm, 60 seconds) an ethanol solution of 0.2 M titanium tetraisopropoxide (TTIP) and annealing at 190°C for 5 minutes. Second, an active mesoporous TiO_2 layer (Dyesol 30NR-T, particle size $\sim 30 \text{ nm}$, $\sim 10 \mu\text{m}$ thick) was coated using the doctor blade technique, followed by heating at 125°C for 10 minutes. Lastly, a scattering layer of TiO_2 (Dyesol WER4-0, particle size $\sim 300 \text{ nm}$, $\sim 5 \mu\text{m}$ thick) was coated on top of the mesoporous TiO_2 layer.

2.2 Synthesis of NaSbSe₂ and device fabrication

The Na-Sb-S precursor was directly grown on a TiO_2 electrode with a single-stage SILAR process. The SILAR growth involved

the following steps: first, the TiO_2 electrode was dipped into a 0.1 M SbCl_3 solution in ethanol for 15 s for Sb^{3+} ionic layer adsorption, followed by rinsing with pure ethanol and drying in air. Second, this electrode was dipped in to a 0.1 M Na_2S solution in methanol for 1 min, followed by rinsing with pure methanol and drying in air. These two steps together are termed as one SILAR cycle. This process was repeated 11 times to grow 11 SILAR cycles of Na-Sb-S precursor. Meanwhile, a Se^{2-} solution was made by dissolving 0.36 g of selenium powder and 0.3 g of NaBH_4 in 125 ml of ethanol under N_2 gas flow. The solution turned from black to colorless within a few minutes, showing the reduction of Se powder to Se^{2-} ion. The Na-Sb-S precursor grown on the TiO_2 electrode was dipped into this solution for the exchange of S^{2-} in the Na-Sb-S structure by Se^{2-} from the solution. Then NaSbSe₂ nanocrystals (NCs) were obtained after annealing the material at 300°C for 40 min under flowing N_2 gas. The NaSbSe₂ NCs were further coated with a ZnSe passivation layer to passivate surface defects according to the procedure described in the literature.²⁸ The solar cells were fabricated by arranging the photoelectrode and counter electrode in a sandwich-type assembly and sealing them with a 190 μm -thick parafilm thermoplastic spacer. Pt and Au-coated FTO substrates were employed as the counter electrodes (CE). Pt CEs were made by dropping a 0.005 M H_2PtCl_6 ethanol solution on an FTO substrate, followed by annealing in a furnace at 400°C for 15 min. This is below the temperature of $\sim 480^\circ\text{C}$ at which cation disorder is induced.²⁴ The Au CE film, $\sim 70 \text{ nm}$ in thickness, was deposited onto an FTO substrate by sputtering. The polysulfide electrolyte consisted of 0.25 M Na_2S , 1 M S, 0.2 M KCl, and 0.1 M KI in a methanol/DI water (volume ratio 7 : 3) solution. The electrolyte was injected separately through a predrilled hole on the counter electrode into the cell.

2.3 Material characterization and photovoltaic measurements

The crystalline structure and phase purity of NaSbSe₂ was analyzed by X-ray diffraction (XRD, Bruker, D8 SSS). Transmission electron microscope (TEM, Joel JEM-2010) was used to determine the crystal size and morphology. Optical property was studied using a Hitachi U-2800A UV-Vis spectrophotometer. The complete ion exchange and elemental analysis was confirmed by energy-dispersive X-ray spectroscopy (EDS coupled SEM, JEOL, JSM-7600F). The photovoltaic performance was studied by measuring photocurrent-voltage ($I-V$) curves using a Keithley 2400 source meter under 100 mW cm^{-2} light illumination from an Oriel 150 W Xe lamp with an Oriel band-pass filter simulating the AM 1.5 solar spectrum. External quantum efficiency (EQE) was measured using the monochromatic light generated from a 250W tungsten halogen lamp.

2.4 First principles calculations

Two structural models were investigated. The first was a monoclinic structure based on the structure of NaSbS_2 , with S replaced by Se and fully relaxed lattice parameters and atomic positions. This model represents the experimental samples studied here. The second model is a model is a special



quasirandom structure (SQS) with cation disorder. We used the reported NaCl structure lattice parameter of 5.966 Å and constructed a 16 atom supercell following the method of Wei and Zunger.²⁹ The atomic coordinates were fully relaxed. The structure relaxations were done using the generalized gradient approximation (GGA) of Perdew, Burke and Ernzerhof (PBE).³⁰ The full relaxation for the monoclinic structure was done using the projector augmented wave (PAW) method as implemented in the VASP code,³¹ with a cut-off energy of 400 eV. All other calculations were done using the linearized augmented plane-wave (LAPW) method as implemented in the WIEN2k code. Electronic structures and optical properties were obtained using the modified Becke-Johnson (mBJ) potential, which generally give improved band gaps compared to the PBE GGA.^{32,33} LAPW spheres of radius 2.3 Bohr were used for all atoms, and spin-orbit was included.

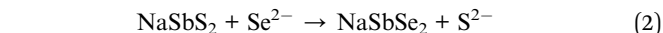
3. Results and discussion

The Na-Sb-S precursor was synthesized based on the reaction between Sb₂S₃ and Na₂S as given in eqn (1) below,³⁴



After annealing the Na-Sb-S precursor under N₂ gas, clear diffraction peaks, shown in Fig. 1 (middle panel), appearing at 16.81, 21.51, 28.60, 30.59, 31.56, 35.40, 43.83, and 45.31° all match well with the (110), (020), (112), (221), (002), (131), (221) and (223) planes of the monoclinic NaSbS₂ reference pattern (JCPDS No. 00-032-1039). There are no other impurity phases observed in the spectrum. The other larger peaks observed belong to either TiO₂ or the FTO substrate (labeled as # in the figure).

The pre-annealed NaSbS₂ precursor was used for S²⁻ exchange with Se²⁻, as demonstrated by eqn (2),



The basis of eqn (2) is explained as follows. The most important factor for driving the ion exchange reaction is the thermodynamic factor. Ions in a solid with a relatively higher solubility can be exchanged by other ions in solution if the product has a lower solubility. The solubility product (K_{sp}) is related to the free energy change of the process. The K_{sp} of metal selenides is lower than that of metal sulfide. Even though the actual solubility can be controlled by many factors, the solubility products of metal chalcogenides have a lower value as the ionic radius of chalcogen increases. That is the ion exchange of S in the crystal with Se²⁻ is thermodynamically feasible process. Once the ion exchange is initiated on the solid-solution interface, further exchange requires the diffusion of ions towards the core of the solid. The inward selenium ion diffusion is accompanied with sulfur ion diffuse towards the solution. In addition, the time required for the exchange reaction is a function of the magnitude of the kinetic barrier for the process.

X-ray diffraction analysis of NaSbSe₂ confirms the successful preparation of single-phase NaSbSe₂ NCs (Fig. 2, top panel). The pronounced NaSbSe₂ peaks are (110), (221), (002), (221), and (223). After conversion to NaSbSe₂, the crystal structure maintained the same monoclinic phase with each (*hkl*) peak shifted to a lower angle relative to the corresponding NaSbS₂ peak. For example, the (002) plane shifted from 31.53 (NaSbS₂) to 30.13 (NaSbSe₂). Our first principles calculations yield lattice parameters, $a = 8.433$ Å, $b = 7.230$ Å, $c = 8.716$ Å, $\gamma = 59.986^\circ$, for a volume 16% larger (~5% linear expansion) than the sulfide, in reasonable accord with these shifts in diffraction peak position. The lower angle shifts are due to lattice expansion as a result of the replacement of smaller S²⁻ (0.184 nm) with larger Se²⁻ (0.198 nm). A size difference of 0.014 nm per atom produces a significant lattice expansion after a complete exchange of S²⁻ with Se²⁻, which is in agreement with the significant lower angle shifts of the NaSbSe₂ peaks relative to the NaSbS₂ peaks. The monoclinic structure found is to be contrasted with that normally obtained by high temperature synthesis, which is NaCl with cation disorder, and partial ordering below 480 °C. The average crystallite size of the NaSbSe₂ NCs, calculated using the Scherrer's equation from the dominant diffraction peak, is

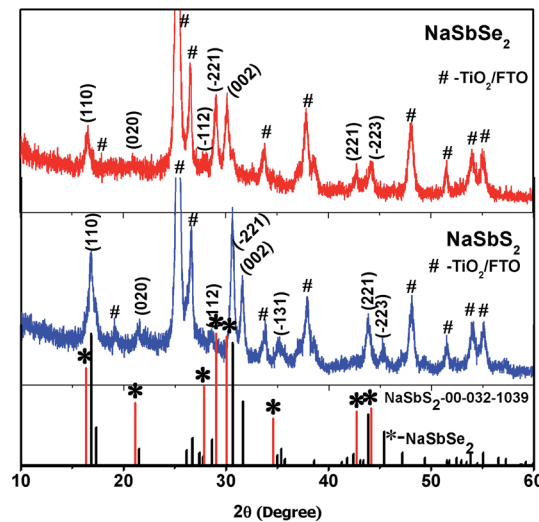


Fig. 1 X-ray diffraction patterns of NaSbSe₂ and NaSbS₂ nanocrystals. Bottom panel: black lines: NaSbS₂ reference pattern; red lines with * symbol: NaSbSe₂ reference pattern.

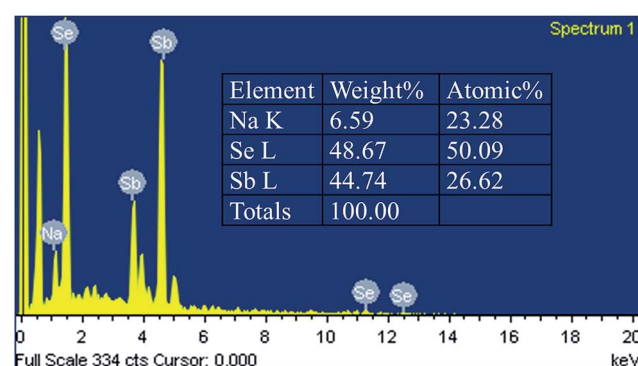


Fig. 2 EDS spectrum of NaSbSe₂ nanocrystals with atomic percentages.



~19 nm, which is close to the size determined from the TEM image shown in Fig. 2 below.

The EDS elemental analysis in Fig. 2 displays the percentage of atoms in the NaSbSe_2 sample. The ratio of $\text{Na} : \text{Sb} : \text{Se} = 1 : 1.14 : 2.15$, in close agreement with the atomic ratio $1 : 1 : 2$ of NaSbSe_2 . The residual amount of sulfur in the sample is undetectable, confirming the complete exchange of S with Se.

The TEM images in Fig. 3 show the synthesized particles prior to and after the ion exchange reaction. Fig. 3(a) shows the NaSbS_2 NCs and Fig. 3(b) shows the NaSbSe_2 NCs deposited on a 30 nm TiO_2 substrate. The NaSbS_2 and NaSbSe_2 NCs have spherical morphology and exhibit no significant changes in

morphology and size after ion exchange. There is no observable aggregation during the SILAR growth of NaSbSe_2 NCs. The NaSbSe_2 NC size ranges from 15–18 nm, with an average diameter of 17 nm.

The first principles density of states and direction averaged optical absorption spectra for the ordered monoclinic structure, representing the experiments, and the disordered SQS model are contrasted in Fig. 4. As seen the electronic structure and optical spectrum are very different for these two structures. NaCl structure NaSbSe_2 with full cation disorder is found to be semimetallic, with an onset of strong optical absorption at 0.5 eV. The ordered monoclinic structure has a calculated indirect band gap of 0.85 eV. The onset of direct optical absorption is at ~1 eV with strong absorption above ~1.5 eV, roughly in accord with the experimental data. Projections of the density of states (not shown) show substantial hybridization between the Se p orbitals making up the valence bands and the nominally unoccupied Sb p orbitals, similar to NaSbS_2 . This type of hybridization favors high mobility due to defect screening, as was discussed previously for NaSbS_2 .²⁷

Fig. 5(a) shows the UV-visible transmission spectra $T(\lambda)$ of three Na–Sb–Se samples: NaSbS_2 , $\text{NaSb}(\text{S}/\text{Se})_2$ and NaSbSe_2 . The three samples were prepared with different ion exchange times of 0, 15 and 40 min, respectively, which changed the crystallographic structures from NaSbS_2 (0 min) to $\text{NaSb}(\text{S}/\text{Se})_2$ (15 min) to NaSbSe_2 (40 min). The transmission edge of NaSbS_2 appears

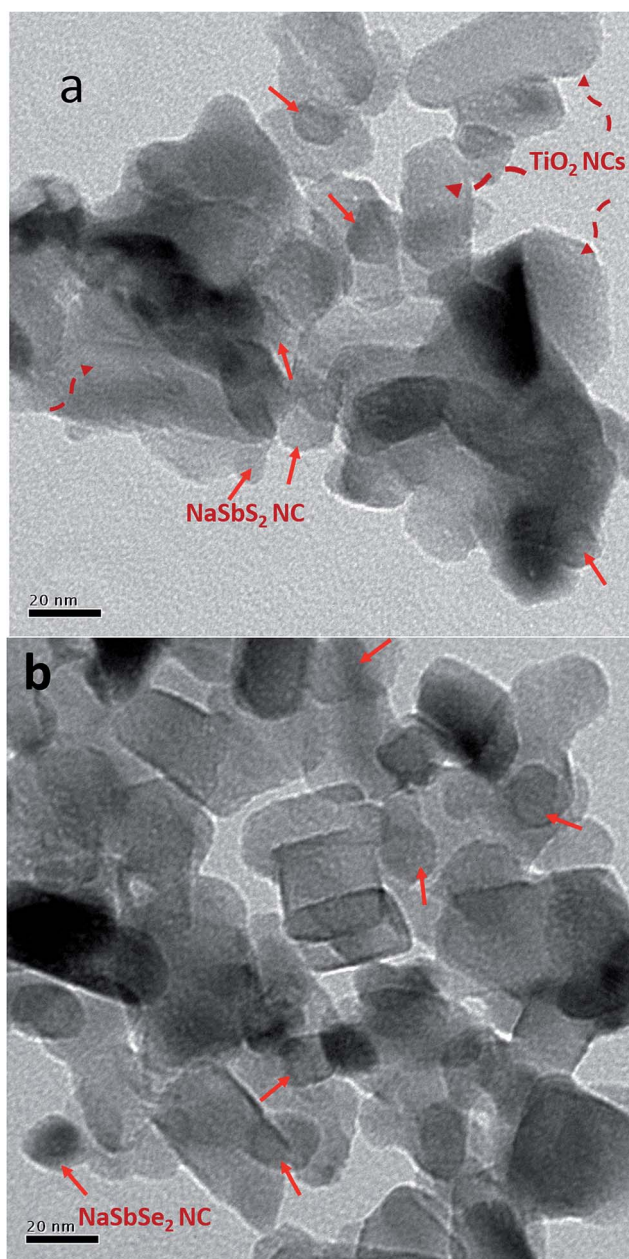


Fig. 3 TEM images of nanocrystals deposited on the surface of TiO_2 : (a) NaSbS_2 and (b) NaSbSe_2 . The red solid arrows mark the NaSbS_2 or NaSbSe_2 NCs while the red-dashed arrows mark TiO_2 particles.

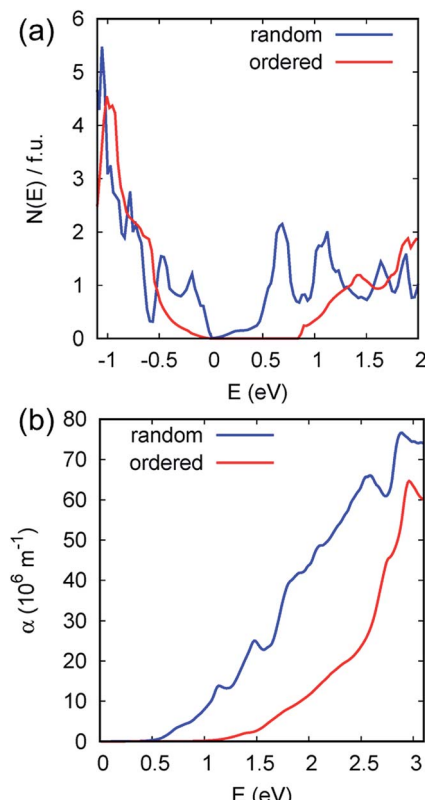


Fig. 4 Calculated electronic density of states (left) and optical absorption (right) for cation disordered and ordered monoclinic NaSbSe_2 as obtained with the mBJ potential. No Drude contribution for semimetallic disordered NaSbSe_2 is included.

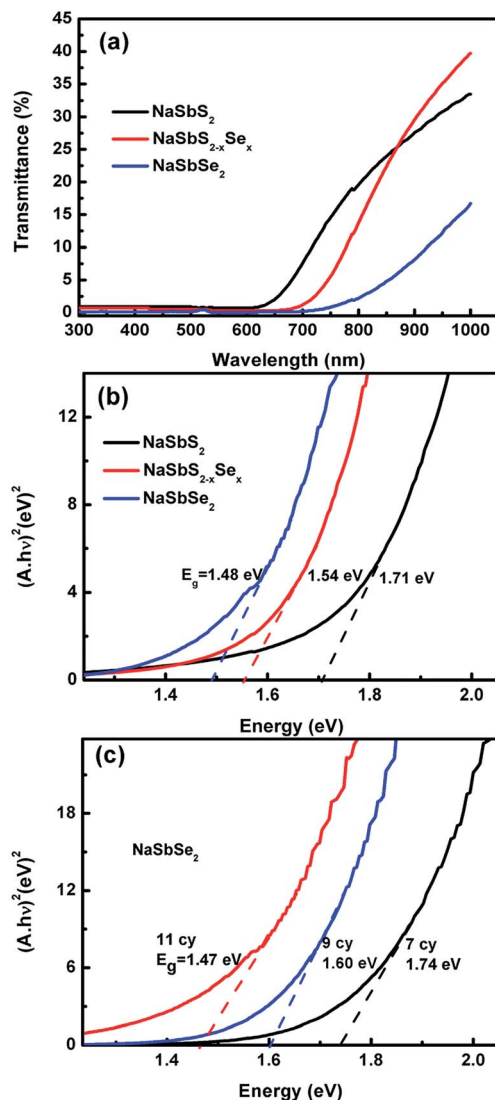


Fig. 5 Optical spectra for NaSbS_2 , $\text{NaSbS}_{2-x}\text{Se}_x$ and NaSbSe_2 NCs: (a) transmission and (b) $(A\text{h}\nu)^2$ vs $\text{h}\nu$ plots. (c) E_g of NaSbSe_2 NCs prepared with different SILAR cycles.

at a higher energy relative to that of the $\text{NaSb}(\text{S}/\text{Se})_2$ and NaSbSe_2 NCs (see Fig. 5(a)). After 15 minutes of S^{2-} ion exchange reaction with Se^{2-} , a significant redshift in transmission edge was observed. A further red shift in transmission edge was observed after 40 minutes of ion exchange. The transmission edge of NaSbSe_2 (determined as the wavelength where $T(\lambda) < 1\%$, *i.e.* absorption = 99%) is ~ 757 nm, while for NaSbS_2 is at a lower wavelength of 630 nm, showing that NaSbSe_2 has a broader absorption range. The energy gaps E_g for NaSbS_2 , $\text{NaSb}(\text{S}/\text{Se})_2$ and NaSbSe_2 NCs were determined from Tauc plots by extrapolating the curves to $y = 0$ as shown in Fig. 5(b). E_g decreases in the order of NaSbS_2 (1.71 eV), $\text{NaSb}(\text{S}/\text{Se})_2$ (1.54 eV), NaSbSe_2 (1.48 eV), in agreement with previous reports.^{23,24} NaSbSe_2 NCs (1.48 eV) have the lowest E_g , resulting in a broader optical absorption range of solar spectrum. The E_g also exhibits a dependence on the particle size of NaSbSe_2 NCs. Fig. 5(c) shows the Tauc plots of three NaSbSe_2 NCs with

different SILAR numbers. The three samples had undergone thorough ion exchange reactions and exhibited the pure NaSbSe_2 phase. A lower SILAR number produces smaller-sized NaSbSe_2 NCs with a higher E_g due to the quantum size effect.³⁵ When the SILAR number is increased from 9, 10 to 11, the size of the NaSbSe_2 NCs would grow larger and the E_g is lowered from 1.74, 1.60 to 1.47 eV, respectively. A notable feature is that the NaSbSe_2 sample with 11 SILAR cycles has an optical E_g of 1.48 eV, which is very close to the optimal E_g of ~ 1.4 eV for a solar absorber,³⁶ suggesting that NaSbSe_2 has the potential to be a highly efficient solar absorber.

3.1 Photovoltaic performance

Fig. 6 shows the I - V curves of NaSbSe_2 QDSSCs for various SILAR cycles n and counter electrodes under 1 sun illumination. The electrolyte used was polysulfide and the counter electrode was Pt. The photovoltaic parameters – short-circuit current density (J_{sc}), fill factor (FF), open-circuit voltage (V_{oc}) and power conversion efficiency (η) are given in Table 1. The SILAR cycles n has a vital effect on the η of the cells. The η of the NaSbSe_2 cells increased when n was increased from 10 to 11 and then decreased when n was further increased to 12 cycles (see Fig. 6 and Table 1, sample nos. 1–3). Therefore the optimum SILAR cycle for NaSbSe_2 QDSSCs is $n = 11$. Surface defects are common problems in SILAR-grown NCs. They act as recombination centers for photogenerated charge carriers. Surface

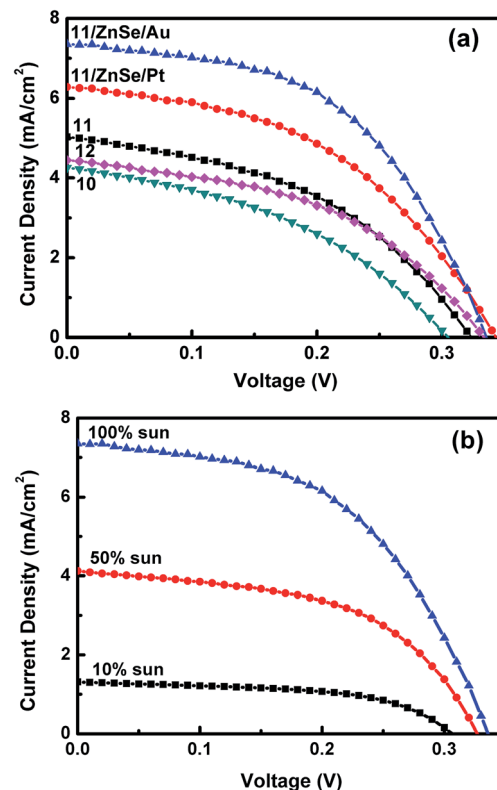


Fig. 6 J - V curves of NaSbSe_2 QDSSCs: (a) with different SILAR cycles and CEs and (b) under various reduced light intensities. CE: Au; electrolyte: polysulfide.

Table 1 NaSbSe₂ QDSSC photovoltaic parameters. Counter electrode (CE): Pt or Au; electrolyte: polysulfide

No	Sample	SILAR cycles <i>n</i>	CE	<i>J</i> _{sc} (mA cm ⁻²)	<i>V</i> _{oc} (V)	FF (%)	η (%)
1	NaSbSe ₂	10	Pt	3.79	0.33	46.1	0.58
2	NaSbSe ₂	11	Pt	5.03	0.32	43.9	0.71
3	NaSbSe ₂	12	Pt	4.25	0.30	41.0	0.52
4	NaSbSe ₂ /ZnSe	11	Pt	6.28	0.34	46.1	0.98
5	NaSbSe ₂ /ZnSe	11	Au	7.35	0.33	51.7	1.25

passivation by a layer of ZnS or ZnSe coating could reduce the density of these defect sites.³⁷ The higher conduction band of ZnSe relative to the conduction band of NaSbSe₂ and TiO₂ acts as an energy barrier and prevents the recombination between the photoelectrons in a NC and holes in the polysulfide electrolyte. The efficiency of NaSbSe₂ QDSSCs with ZnSe passivation improved from 0.71% (before) to 0.98% (after) (see Fig. 5(a) and Table 1, sample no. 4), an increase of 38%. The efficiency improvement is the result of combined contributions from enhanced *J*_{sc}, FF and *V*_{oc}. The effect of counter electrodes (CEs) on the performance of the NaSbSe₂ cells was analyzed by employing two types of CEs – Pt and Au. The cell with Au CE exhibited a higher η of 1.25% (sample no. 5), a 27% enhancement relative to Pt CE (0.98%). This is mainly a result of improved *J*_{sc} = 7.35 mA cm⁻² and FF = 51.7% with Au CE relative to Pt CE (*J*_{sc} = 6.28 mA cm⁻² and FF = 46.1). In a polysulfide electrolyte, a Pt CE has lower electrocatalytic activity relative to an Au CE towards reduction of the electrolyte. This is due to sulfide poisoning of the catalytic active sites of a Pt CE.³⁸

Fig. 6(b) displays the *I*–*V* curves of NaSbSe₂ QDSSCs with Au CE under various reduced light intensities. Table 2 presents the corresponding solar cell parameters. The η increased to 2.22% as the intensity was reduced to 10% sun, a 78% increase over the 1.25% under 1 sun. Moreover, the normalized *J*_{sc} increased to 13.1 mA cm⁻², which is significantly larger than *J*_{sc} = 7.35 mA cm⁻² under 1 sun. The improvement in the photovoltaic performance – *J*_{sc}, FF and η – under reduced light intensities is attributed to a reduced photoelectron–hole recombination rate. The electron–hole (e–h) recombination rate is proportional to the number of e–h pairs generated by the incident light. Under a low light intensity, the absorber generates fewer charge carriers, leading to reduced recombination and improved *J*_{sc}, FF and η . The significantly improved η under low light intensities indicates that carrier recombination is an active process in the NaSbSe₂ QDSSCs.

The efficiency (2.22%) of the present NaSbSe₂ cells is lower than that (3.18%) observed in NaSbS₂ cells.²³ The different efficiencies are caused mainly by the different open-circuit

Table 2 NaSbSe₂ QDSSC photovoltaic parameters under various reduced sun intensities. CE: Au; electrolyte: polysulfide. The *J*_{sc} in brackets represents the photocurrent normalized to one sun

Sun power	<i>J</i> _{sc} (mA cm ⁻²)	<i>V</i> _{oc} (V)	FF (%)	η (%)
100%	7.35	0.33	51.7	1.25
50%	4.12 (8.24)	0.32	53.5	1.41
10%	1.31 (13.1)	0.30	56.4	2.22

voltage *V*_{oc}s: 0.33 V in NaSbSe₂ and 0.45 V in NaSbS₂. *V*_{oc} is proportional to the energy gap *E*_g. As revealed in the present work, NaSbSe₂ has a smaller *E*_g (\sim 1.45 eV) than that (1.8 eV) of NaSbS₂. The smaller *E*_g in NaSbSe₂ leads to a smaller *V*_{oc} and, hence, a smaller efficiency, as shown in this work. The *J*_{sc} of NaSbSe₂ (7.35 mA cm⁻²) is smaller than that of NaSbS₂ (10.76 mA cm⁻²). In principle, the smaller *E*_g in NaSbSe₂ should produce a larger *J*_{sc} than that in NaSbS₂ with a larger *E*_g. The reason for the lower *J*_{sc} is probably due to the surface defects formed on the surface of NaSbSe₂ NCs during the ion-exchange reaction. The higher density of surface defects in NaSbSe₂ relative to that in NaSbS₂ results in a lower *J*_{sc}. With improved material growth, the problem of surface defects could be reduced and the *J*_{sc} in NaSbSe₂ should eventually surpass the *J*_{sc} in NaSbS₂.

The EQE spectrum covers the spectral range from 300 to 900 nm with the maximum value of 75% at λ = 550 nm, as plotted in Fig. 7. The energy gap of NaSbSe₂, determined from the onset of the EQE curve, is *E*_g \sim 1.38 eV, in close agreement with the value (1.48 eV) determined from optical measurements (Fig. 5). Therefore, we conclude based on the optical and EQE data that the *E*_g of the material is in the range of \sim 1.4–1.5 eV. The EQE integrated current density *J*_{ph}, the total photocurrent that the cell can generate, can be determined from the following equation:

$$J_{\text{ph}} = e \int_{300}^{900} \Phi(\lambda) \text{EQE}(\lambda) d(\lambda)$$

where $\Phi(\lambda)$ is the incident light intensity and *e* is the elementary charge. The integrated photocurrent plotted in the right axis of Fig. 7 yields a total *J*_{ph} of 14.5 mA cm⁻². This is in close agreement with the normalized *J*_{sc} = 13.1 mA cm⁻² from the *I*–*V* result (see Table 2).

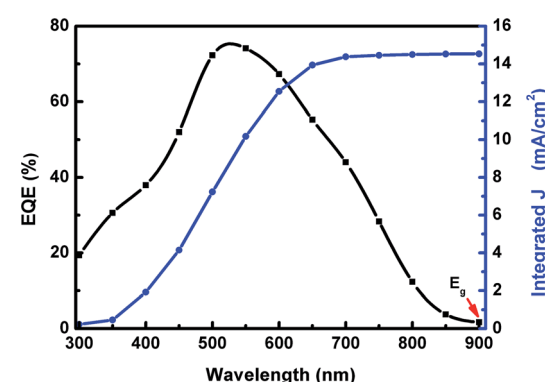


Fig. 7 EQE spectrum.



We summarize the notable results in this work. NaSbSe_2 NCs were synthesized from the NaSbS_2 precursor using the ion exchange method. The synthesized NaSbSe_2 has larger lattice constants as well as a reduced optical E_g (1.48 eV) compared to that of the parent NaSbS_2 . This E_g is very close to the optimal E_g of a solar absorber. First principles calculations show that the synthesis method is crucial in yielded NCs with cation order and in particular that the cation disorder in material grown at high temperature will be detrimental. The best cell exhibited an efficiency of 2.2% under 0.1 sun, a respectable value for the first report of a new solar material. Since the synthesis method is a general technique, many new ternary metal selenide-based solar materials can be produced following the same technique used in this work.

4. Conclusion

In summary, we have successfully synthesized NCs from the as-synthesized Na-Sb-S precursor by the solution-phase Se^{2-} -anion exchange reaction. A reaction time of 40 min completed the NaSbS_2 to NaSbSe_2 exchange reaction. NaSbSe_2 NCs exhibit the same crystal structure as the parent NaSbS_2 precursor with larger lattice constants and a lower E_g of 1.48 eV relative to NaSbS_2 (1.71 eV). The best solar cell was prepared using 11 SILAR cycles, an Au counter electrode and a ZnSe passivation coating. The best cell exhibits a normalized $J_{sc} = 13.1 \text{ mA cm}^{-2}$, a $V_{oc} = 0.30 \text{ V}$, a $FF = 56.4\%$ and an $\eta = 2.22\%$. The near-optimal E_g suggests that NaSbSe_2 has the potential to be a highly efficient solar material.

Conflicts of interest

There is no conflict to declare.

Acknowledgements

The authors are grateful to the financial support from the Ministry of Science and Technology of the Republic of China under grant Nos. MOST 103-2112-M-005-004-MY3 and MOST 105-2811-M-005-008. Work at the University of Missouri was supported by the U.S. Department of Energy through the S3TEC Energy Frontier Research Center, Award Number DE-SC0001299/DEFG02-09ER46577.

References

- 1 P. V. Kamat, *J. Phys. Chem. C*, 2008, **112**, 18737–18753.
- 2 J. Tian and G. Cao, *J. Phys. Chem. Lett.*, 2015, **6**, 1859–1869.
- 3 V. González-Pedro, X. Xu, I. Mora-Seró and J. Bisquert, *ACS Nano*, 2010, **4**, 5783–5790.
- 4 J. Tian, T. Shen, X. Liu, C. Fei, L. Lv and G. Cao, *Sci. Rep.*, 2016, **6**, 23094.
- 5 R. J. Ellingson, M. C. Beard, J. C. Johnson, P. Yu, O. I. Micic, A. J. Nozik, A. Shabaev and A. L. Efros, *Nano Lett.*, 2005, **5**, 865–871.
- 6 M. Green, in *Third Generation Photovoltaics: Advanced Solar Energy Conversion*, Springer Berlin Heidelberg, Berlin, Heidelberg, 2003, DOI: 10.1007/3-540-26563-5_3, pp. 21–34.
- 7 S. N. Guin, A. Chatterjee, D. S. Negi, R. Datta and K. Biswas, *Energy Environ. Sci.*, 2013, **6**, 2603–2608.
- 8 S. N. Guin, V. Srihari and K. Biswas, *J. Mater. Chem. A*, 2015, **3**, 648–655.
- 9 S. N. Guin and K. Biswas, *Chem. Mater.*, 2013, **25**, 3225–3231.
- 10 C. Xiao, X. Qin, J. Zhang, R. An, J. Xu, K. Li, B. Cao, J. Yang, B. Ye and Y. Xie, *J. Am. Chem. Soc.*, 2012, **134**, 18460–18466.
- 11 C.-L. Chou, N. Suriyawong, B. Aragaw, J.-B. Shi and M.-W. Lee, *J. Electrochem. Soc.*, 2016, **163**, H445–H449.
- 12 N. Liang, W. Chen, F. Dai, X. Wu, W. Zhang, Z. Li, J. Shen, S. Huang, Q. He, J. Zai, N. Fang and X. Qian, *CrystEngComm*, 2015, **17**, 1902–1905.
- 13 Z. Liu, J. Huang, J. Han, T. Hong, J. Zhang and Z. Liu, *Phys. Chem. Chem. Phys.*, 2016, **18**, 16615–16620.
- 14 M. Bernechea, N. C. Miller, G. Xercavins, D. So, A. Stavrinadis and G. Konstantatos, *Nat. Photonics*, 2016, **10**, 521–525.
- 15 N. Suriyawong, B. Aragaw, J.-B. Shi and M.-W. Lee, *J. Colloid Interface Sci.*, 2016, **473**, 60–65.
- 16 P.-C. Huang, W.-C. Yang and M.-W. Lee, *J. Phys. Chem. C*, 2013, **117**, 18308–18314.
- 17 M. Kumar and C. Persson, *IRESR*, 2013, vol. 5, p. 031616.
- 18 K. Ramasamy, B. Tien, P. S. Archana and A. Gupta, *Mater. Lett.*, 2014, **124**, 227–230.
- 19 S. Dekhil, H. Dahman, S. Rabaoui, N. Yaacoub and L. El Mir, *J. Mater. Sci.: Mater. Electron.*, 2017, **28**, 11631–11635.
- 20 L. Wang, C. Ma, K. Hu, R. Zhou, X. Mao, S. Pan, L. H. Wong and J. Xu, *J. Alloys Compd.*, 2016, **680**, 182–190.
- 21 W. Septina, S. Ikeda, Y. Iga, T. Harada and M. Matsumura, *Thin Solid Films*, 2014, **550**, 700–704.
- 22 W.-C. Yang and M.-W. Lee, *J. Electrochem. Soc.*, 2014, **161**, H92–H96.
- 23 S. U. Rahayu, C.-L. Chou, N. Suriyawong, B. A. Aragaw, J.-B. Shi and M.-W. Lee, *APL Mater.*, 2016, **4**, 116103.
- 24 V. A. Bazakutsa, N. I. Gnidash, A. K. Kul'chitskaya and A. V. Salov, *Phys. Usp.*, 1975, **18**, 472–475.
- 25 M. D. Nielsen, V. Ozolins and J. P. Heremans, *Energy Environ. Sci.*, 2013, **6**, 570–578.
- 26 S. I. Berul', Y. G. Finkel'shtein and N. P. Luzhnaya, in *Chemical Bonds in Solids: Semiconductor Crystals, Glasses, and Liquids*, ed. A. N. N. Sirota, Springer US, Boston, MA, 1995, vol. 4, DOI: 10.1007/978-1-4684-8682-7_28, pp. 149–154.
- 27 J. Sun and D. J. Singh, *Phys. Rev. Appl.*, 2017, **7**, 024015.
- 28 F. Huang, J. Hou, Q. Zhang, Y. Wang, R. C. Massé, S. Peng, H. Wang, J. Liu and G. Cao, *Nano Energy*, 2016, **26**, 114–122.
- 29 S. H. Wei and A. Zunger, Disorder Effects on the Density of States of the II-VI Semiconductor Alloys $\text{Hg}_{0.5}\text{Cd}_{0.5}\text{Te}$, $\text{Cd}_{0.5}\text{Zn}_{0.5}\text{Te}$ and $\text{Hg}_{0.5}\text{Zn}_{0.5}\text{Te}$, *Phys. Rev. B: Condens. Matter Mater. Phys.*, 1991, **43**, 14272.
- 30 J. P. Perdew, K. Burke and M. Ernzerhof, Generalized Gradient Approximation Made Simple, *Phys. Rev. Lett.*, 1996, **77**, 3865.



31 G. Kresse and D. Joubert, From Ultrasoft Pseudopotentials to the Projector Augmented-Wave Method, *Phys. Rev. B: Condens. Matter Mater. Phys.*, 1999, **59**, 1758.

32 F. Tran and P. Blaha, Accurate Band Gaps of Semiconductors and Insulators with a Semilocal Exchange–Correlation Potential, *Phys. Rev. Lett.*, 2009, **102**, 226401.

33 D. J. Singh, Electronic Structure Calculations with the Tran–Blaha Modified Becke-Johnson Density Functional, *Phys. Rev. B: Condens. Matter Mater. Phys.*, 2010, **82**, 205102.

34 C. A. Jacobson, E. C. Weaver and C. A. Hampel, *Encyclopedia of chemical reactions*, Reinhold Pub. Corp., New York, 1946.

35 S. Gorer and G. Hodes, *J. Phys. Chem.*, 1994, **98**, 5338–5346.

36 T. Zdanowicz, T. Rodziewicz and M. Zabkowska-Waclawek, *Sol. Energy Mater. Sol. Cells*, 2005, **87**, 757–769.

37 F. Huang, Q. Zhang, B. Xu, J. Hou, Y. Wang, R. C. Masse, S. Peng, J. Liu and G. Cao, *J. Mater. Chem. A*, 2016, **4**, 14773–14780.

38 G. Hodes, J. Manassen and D. Cahen, *J. Electrochem. Soc.*, 1980, **127**, 544–549.

